Behaviour of Confined n-Alkanes under High Pressures and Shear Rates: A Nonequilibrium Molecular Dynamics Study

Sebastián Echeverri Restrepo[a,b], Marcel van Eijk[a], James P. Ewen[c]

[a]*SKF Research & Technology Development, Nieuwegein, The Netherlands*
[b]*Department of Physics, King's College London, Strand, London WC2R 2LS, UK*
[c]*Department of Mechanical Engineering, Imperial College London, London SW7 2AZ, England, UK*

Abstract

In this study, the behaviour of n-alkanes confined and sheared between iron oxide surfaces has been investigated using nonequilibrium molecular dynamics simulations. The chain extension and orientation, film structure and flow, and friction have been measured at various applied pressures and shear rates representative of the elastohydrodynamic lubrication regime. The effect of increasing n-alkane chain length has also been investigated. At higher pressure, the films show more layering and ordering, suggesting that they become more solid-like. Conversely, at higher shear rates, the chains become less elongated, aligned, layered, and ordered; indicating the films become more liquid-like as the temperature of the film increases. Long chains are generally more solid-like, in accordance with their lower melting point. Long chains, with higher viscosity give higher friction, particularly at low shear rates. For short chains, the flow remains mostly Couette-like under all of the conditions studied, with some boundary slip at the highest shear rates studied. However, long chains show rich nonequilibrium phase behaviour. Friction is generally more sensitive to pressure than chain length in the ranges studied. At low pressure, friction increases linearly with logarithmic shear rate, at intermediate pressure, friction becomes insensitive to shear rate, and at high pressure, friction decreases with increasing shear rate. The results of this study have shown how the nanoscale structure and flow behaviour of lubricants under extreme conditions can deviate from that which is commonly assumed, leading to an unusual frictional response.

1. Introduction

From polymer processing to the design of microfluidic devices, the behaviour of fluids confined and sheared between solid surfaces is of broad industrial interest. A detailed understanding of this behaviour is particularly critical in tribology, where lubricant films are used to separate moving surfaces to minimise friction and wear. In lubricated machine components that are based on elements that roll and slide together (e.g. rolling bearings, gears, constant velocity joints and cam/follower systems) a significant portion of the friction losses originate from the elastohydrodynamic lubrication (EHL) regime. In the EHL regime, thin lubricant films are subjected to very high pressures (GPa) and shear rates ($> 10^7 \, \mathrm{s}^{-1}$). These conditions are challenging to probe directly through experiment, and thus the behaviour of lubricants under EHL conditions remains somewhat unclear [1].

Alongside experiments, nonequilibrium molecular dynamics (NEMD) simulations can provide unique insights into the behaviour of lubricants under EHL conditions [2]. Since the early 1990s, many studies have investigated the behaviour of lubricants strongly confined (< 6 molecular layers) between solid surfaces, where confinement is known to significantly increase viscosity [3]. Early NEMD simulations of thin atomic and molecular fluid films suggested that this viscosity increase was due to vitrification to a glassy state or even crystallization [4]. They also showed flow behaviour that deviated from the linear (Couette) case, such as boundary slip as well as slip between molecular layers within the fluid film itself [5]. NEMD comparisons between thin (8 molecular layers) films of different n-alkane chain lengths ($C_6 - C_{80}$) suggested that, at low pressure ($0.1 \, \mathrm{MPa}$), interlayer slip within the ordered film occurred and shear stress was sensitive to the chain length [6]. Conversely, at high pressure ($100 \, \mathrm{MPa}$), boundary slip occurred and the shear stress was insensitive to the chain length [6]. The shear stress was also found to be dependent on chain length ($C_{20} - C_{1400}$) for thin (7 molecular layers) n-alkane films sheared between polymer-like surfaces (no-slip) at low pressure ($10 \, \mathrm{MPa}$) [7]. However, for metal-like surfaces (slip), the shear stress was independent on the chain length under the same conditions [7]. For the same systems, the shear stress was also shown to increase monotonically with the sliding velocity for metal-like surfaces but to be independent of sliding velocity on polymer-like surfaces [8]. It was also found that shorter (C_{20}) chains melt under shear, whereas longer chains only showed thermal softening [9].

Relatively fewer NEMD studies have investigated the

behaviour of thicker lubricant films (≥ 10 molecular layers) of direct relevance to EHL. Both NEMD simulations [4, 11] and experiments [12] have suggested that there could be similarities between the behaviour of strongly confined films and thicker films subjected to high pressures. Indeed, comprehensive NEMD simulations of relatively thick (35 atomic layers) atomic fluid films showed nonequilibrium phase behaviour under high shear rate and pressure conditions [13, 14] which was reminiscent of previous observations of more strongly confined films at lower pressure [5]. Further NEMD simulations showed that the nonequilibrium phase transitions observed at high pressure can lead to deviations from classical friction laws [15], which has also been observed for thinner alkane films at lower pressure [8]. Recently, unusual friction and nonequilibrium phase behaviour has also been observed in NEMD simulations of relatively thick films of model lubricant and traction fluid molecules under EHL conditions [16]. To design new lubricant molecules to control EHL friction, it is of significant interest to assess how the friction and nonequilibrium phase behaviour changes with molecular structure, for example chain length.

In the present study, the behaviour of n-alkanes confined and sheared between Fe_2O_3 surfaces (as a model for steel) has been investigated under EHL conditions using NEMD simulations. The effect of n-alkane chain length ($C_{16} - C_{60}$), applied pressure ($0.5 - 1.5$ GPa) and shear rate ($10^9 - 10^{10}$ s^{-1}) on the chain extension and orientation, film structure and flow, and friction has been studied. These results shed further light on the behaviour of model lubricants under EHL conditions.

2. Methodology

Classical MD simulations were performed using the large-scale atomic/molecular massively parallel simulator (LAMMPS) software [17]. The velocity-Verlet algorithm was used to integrate the equations of motion with a time-step of 1.0 fs. All of the initial configurations were generated using the open source LAMMPS_builder software [18, 19], which utilizes Moltemplate [20] and the Atomic Simulation Environment (ASE) [21]. The systems consist of two parallel atomically-smooth surfaces separated an approximately 8 nm thick n-alkane lubricant layer, see Figure 1. The n-alkane layer was sufficiently thick (≥ 16 molecular layers) such that the lubricant was not strongly layered in the middle of the film (see Figure 7) and thus any confinement-induced viscosity increase was expected to be negligible [22]. Periodic boundary conditions were applied in the x and y directions.

The lubricant layer consisted of n-alkanes of different lengths: n-hexadecane (C_{16}), n-triacontane (C_{30}) and n-hexacontane (C_{60}). For all the cases, a total number of 19200 carbon atoms were inserted into the system; this corresponds to 1200, 640 and 320 molecules for C_{16}, C_{30} and C_{60}, respectively. Lubricant molecules are usually in

the middle of this range, with n-alkanes constituting a significant proportion of modern engine oils [23].

Parameters from the long hydrocarbon-optimized potentials for liquid simulations, all-atom force field (L-OPLS-AA) [24, 25] were used for the carbon and hydrogen atoms in the alkane chains. This force-field has been shown to correctly describe the viscous behaviour of long alkanes under ambient and high temperature, high pressure conditions [26]. All-atom force-fields have also been shown to be important to accurately model phase transitions in confined alkane systems [27]. Cross-interactions were evaluated using the geometric mean mixing rules [24]. All C-H bonds were constrained using the SHAKE algorithm [28]. Lennard-Jones interactions were cut off at 12 Å and electrostatic interactions were evaluated using a slab implementation of the particle-particle-particle-mesh (PPPM) algorithm [29] with a relative accuracy in the forces of 1×10^{-7}.

Hematite (Fe_2O_3) slabs were chosen as a representative model for steel surfaces [30]. The hematite slabs [31] were cleaved and oriented such that the [001] plane points towards z and [100] points towards x (see Figure 1). The thickness of the surfaces in the z direction is 13.73 Å and the size of the surface in the x and y directions are 80.46 Å and 78.39 Å respectively. The cell dimensions were large enough to prevent the interaction of individual n-alkane chains with their own periodic image. The Fe and O surface atoms are restrained in the corundum crystal structure [31] with harmonic bonds between atoms within 3 Å. The force constant of these bonds was 130 kcal mol^{-1} Å^{-2}, which has been shown previously to keep the surface structure suitably rigid but not to adversely affect the thermostatting [32]. The surface Fe and O Lennard-Jones [10] and partial charge [32] parameters, which determine the strength of the interactions with the lubricant atoms, were specifically developed to simulate alkane behaviour on hematite surfaces.

2.1. Equilibration

First, n-alkane molecules were inserted between the slabs in an ordered fashion, followed by energy minimisation. Next, a properly equilibrated system was a generated using a simple heat-quench sequence. In this procedure, the initially ordered alkanes were heated to 2000 K to accelerate diffusion, and left to evolve until equilibrium is reached (10 ns). The system was then quenched back to the target temperature 353 K over a further 10 ns. During the heat-quench sequence, the fluid temperature was controlled using a global Langevin thermostat [33], with a damping constant of 0.1 ps, acting in all directions.

Three different criteria were considered to ensure that the systems had reached equilibrium. Specifically, verifying that the mean square end-to-end distance ($\langle R^2 \rangle$) and the mean square radius of gyration ($\langle S^2 \rangle$) reached a steady state [34]. The final criterion reflects the fact that systems of long chain alkanes which are not properly equi-

librated can present deformation on short length scales, and this deformation is only relaxed after the chains have moved a distance equivalent to their own size [35]. In order to verify this, the mean-squared displacement for the C atoms (MSD_{atom}) and for the centre of mass of the alkane chains (MSD_{CG}) were also monitored during equilibration. More details regarding the equilibration procedure can be found in the Appendix. The final equilibrated configurations were used as inputs for the following compression and shear simulations.

2.2. Compression

After the systems were properly equilibrated, the pressure was increased by giving a uniform normal force to the outer layer of Fe atoms in the top wall while keeping the outer layer of atoms in the bottom wall fixed in the z direction (see Figure 1). Three different pressure values were considered; 0.5 GPa, 1.0 GPa, and 1.5 GPa. These are of direct relevance to the EHL regime [1].
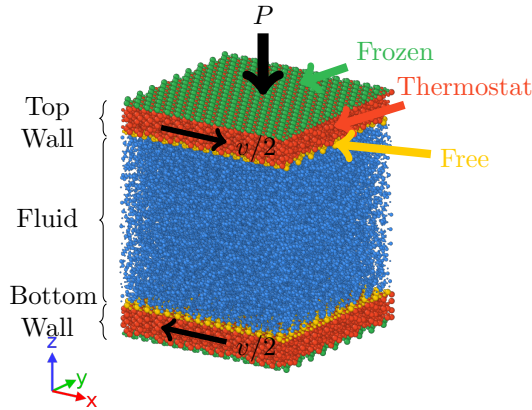

Figure 1: Structure and regions of a typical system for the simulation of confined lubricants. The system is divided in three regions, namely, the fluid, and the top and bottom walls. Within each wall, the *frozen* atoms (green) are used to apply the shearing and compressive constraints, and the *thermostat* atoms (orange) to control the temperature. Both the *free* (yellow) and fluid (blue) atoms are left unconstrained.

For the compression and shearing stages, the temperature of the system is controlled (T = 353 K) by a Langevin thermostat [33] with a damping constant of 0.1 ps acting only on the middle layer of atoms in the slabs (*thermostat* in Figure 1). The thermostat was applied only in the direction perpendicular to both the sliding and compression (y). This approach is known to be more physically meaningful than applying the thermostat directly to the confined fluid, which has been shown to significantly affect friction and flow behaviour, particularly at high shear rates [36, 37, 38].

The compression phase is performed in two steps; first, the pressure is linearly incremented over 10 ns and then the target pressure is maintained for a further 10 ns. The density of the fluid region and the average pressure reach a steady state well within the simulation time. The different

Table 1: Effect of confined n-alkane chain length and pressure on the average density in the fluid region (1)

	$\rho\,[\text{kg m}^{-3}]$		
P [GPa] Chain Length	0.5	1.0	1.5
C_{16}	0.87	0.93	0.98
C_{30}	0.90	0.96	1.00
C_{60}	0.91	0.97	1.01

final densities are presented in Table 1 which correspond to the average density of the final 1 ns of the compression phase. In agreement with the available experimental data [39], there is an increase in average density with increasing alkane chain length, as well as with increasing pressure.

2.3. Shear

After the n-alkanes are equilibrated at the target pressures ($0.5 - 1.5$ GPa), the shear response of the lubricant was studied. A shear velocity gradient was imposed on the system by means of a constant velocity, $v_x = \pm v_s/2$ applied to the outermost layer of atoms in each slab (see Figure 1) in the x direction. The following sliding velocities were considered, v_s; $10\,\text{m s}^{-1}$, $20\,\text{m s}^{-1}$, $50\,\text{m s}^{-1}$ and $100\,\text{m s}^{-1}$. For the simulated film thickness (approx. 8 nm), these correspond to applied shear rates, $\dot{\gamma}$, of approximately $10^9 - 10^{10}\text{s}^{-1}$. While these are above those encountered in real engineering components $(10^6 - 10^8\text{s}^{-1})$ [40], lower shear rates do not reach a steady state in the available simulation time for the longer chains studied [2].

To verify that a nonequilibrium steady state was reached, the evolution of the mean square end-to-end distance ($\langle R^2 \rangle$), the segmental orientation ($\langle P_2^{xz} \rangle$) [41] and the shear stress (σ) on the surfaces in response to the fluid, were monitored. Lower sliding velocities require a longer simulation time to reach a steady state; however, they require a similar sliding distance, in agreement with experimental observations [42]. In general, a steady state is reached in a shorter sliding distance for shorter alkanes and lower pressures. A representative case is C_{30} at 1.0 GPa, for which the evolution of $\langle R^2 \rangle$, $\langle P_2^{xz} \rangle$, and σ are presented at four sliding velocities in Figure 2.

Since the initial configuration is the same for all of the sliding velocities, they all have an initial value of $\langle R^2 \rangle = 283\,\text{Å}^2$. After this point, $\langle R^2 \rangle$ increases and then asymptotes towards a steady state value. This suggests that the chains generally unfold when shear is applied. The steady state $\langle R^2 \rangle$ is lower at higher sliding velocity, as has been observed in previous simulations of similar systems at high shear rates [43].

For ideal chains in the bulk, the average segmental orientation, $\langle P_2^{xz} \rangle = 0.25$. This suggests a uniform distribution of the orientation of the chains, which corresponds to
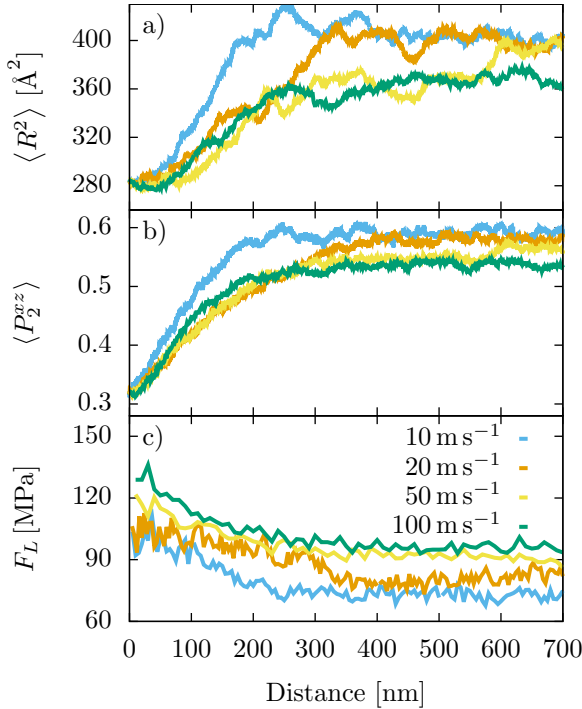
an average orientation angle of 45°. When under confinement, n-alkane molecules close to the surfaces tend to align parallel to them [43], meaning that the angle between the chain and the surface is close to zero, and hence $\langle P_2^{xz}\rangle$ increases. In the case of C_{30} at 1.0 GPa, $\langle P_2^{xz}\rangle = 0.32$ before shear is applied (see Figure 2b), indicating that there is a preferential orientation caused by the presence of the surfaces. When sliding is initiated, the chains begin to align with the flow direction, increasing $\langle P_2^{xz}\rangle$.

The shear stress was monitored through the average lateral (friction) force F_L acting on the outermost layer of atoms (frozen atoms in Figure 1) in the top and bottom slabs (divided by their area) in response to the fluid. At the onset of sliding, F_L increases rapidly to reach a maximum value and then decreases before reaching a steady state, indicating stress overshoot behaviour[44]. The sliding distance needed for F_L to reach a steady state is consistent with that needed for $\langle R^2\rangle$ and $\langle P_2^{xz}\rangle$ (Figure 2).

Once the simulations reach a steady state (Figure 2), they are run for a further 5 ns to 20 ns while maintaining a constant sliding velocity and applied pressure. During the final 2 ns of the simulation, $\langle R^2\rangle$, $\langle P_2^{xz}\rangle$, and σ are measured and averaged. The results are presented and discussed in the next section.

3. Results and Discussion

3.1. Chain extension and orientation

Longer chains will inherently have higher absolute values of $\langle R^2\rangle$, so to compare the variation of $\langle R^2\rangle$ between the different chain lengths, the mean square end-to-end distance *per C-C bond*; $\langle R^2\rangle / (N_{\mathrm{bonds}})^2$ was calculated to normalize between the different chain lengths studied. The steady state $\langle R^2\rangle$ per C-C bond is presented as a function of shear rate for the different chain lengths and pressures studied in Figure 3.

For the chain lengths and pressures studied, $\langle R^2\rangle / (N_{\mathrm{bonds}})^2$ generally decreases with increasing shear rate, suggesting less extended chain conformations. This has also been observed in previous bulk [45] and confined [7, 43] NEMD simulations of similar n-alkanes at high shear rates. This decrease has been attributed to strong intermolecular collisions which lead to intense chain rotation and tumbling dynamics at higher shear rates [43]. However, long chains at high pressure show the opposite trend. Longer chains are relatively less extended than shorter chains at all pressures and shear rates studied. The chains are slightly less extended at higher pressure, although this is only discernible at low shear rates.

Surprisingly, there is also a general reduction of $\langle P_2^{xz}\rangle$ with increasing shear rate (see Figure 4). This indicates an increase of the average angle of segments relative to the shearing direction at higher shear rate (see Appendix), meaning that the chains are less aligned with flow direction. Although such behaviour has also been observed in bulk NEMD simulations of n-alkanes at high shear rates [46],

Figure 2: Evolution of the a) mean square end-to-end distance ($\langle R^2\rangle$), b) the average segmental orientation ($\langle P_2^{xz}\rangle$), c) the lateral (friction) force (σ) and d) the temperature (T) for a system with alkane chains of length C_{30} at a pressure of 1.0 GPa and four shearing velocities. The transient state begins with the application of the shear displacement of the surfaces and ends when steady state is attained. Note that 1×10^6 steps correspond to 1 ns.
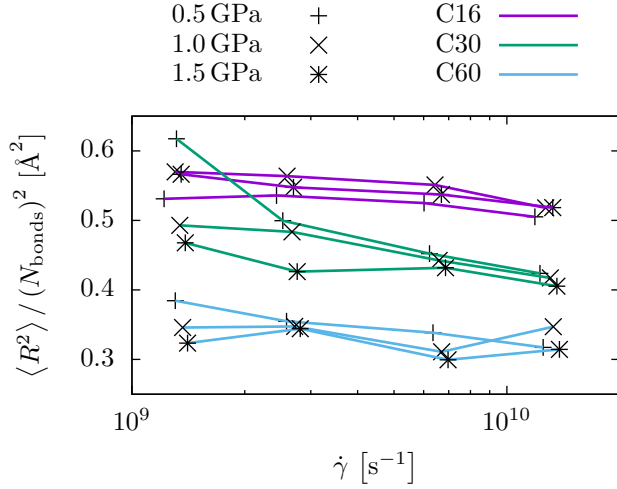
Figure 3: Mean square end-to-end distance ($\langle R^2 \rangle$) per C-C bond as a function of the shear rate ($\dot{\gamma}$). Error bars, calculated from the standard deviation between block-averages, are omitted for clarity, but are of a similar size to the symbols.
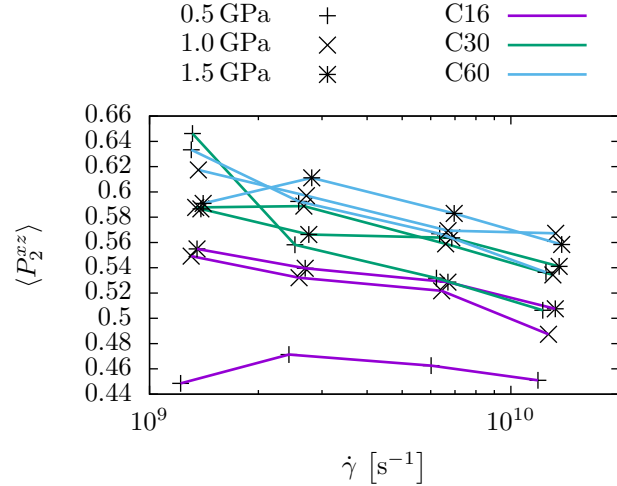

Figure 4: Average segmental orientation as a function of the shear rate ($\dot{\gamma}$). Error bars, calculated from the standard deviation between block-averages, are omitted for clarity, but are of a similar size to the symbols.

the opposite trend is more commonly reported [43, 45]. This discrepancy can be rationalised through the high pressures applied in these simulations which lead to the fluid becoming solid-like, which is discussed further in the following section. Previous experiments [47] and NEMD simulations [43] have shown that n-alkanes close to the confining walls align with the shear direction. Under the high pressures applied in these NEMD simulations, the ordered region extends further towards the centre of the film (Figure 7), leading to a high value of $\langle P_2^{xz} \rangle$. As the shear rate is increased, the film becomes more liquid-like (Figure 5), and the thickness of the ordered region decreases (Figure 7), and thus $\langle P_2^{xz} \rangle$ also decreases. Consistent with previous bulk NEMD simulations [45], longer chains tend be more aligned with the shearing direction, while the chains are slightly less aligned at higher pressure.

3.2. Film structure and flow

The radial distribution function (RDF), $g(r)$ for the C atoms was calculated using a cut-off distance of 20 Å (see Figure 5). Note that atoms separated by one or two bonds were excluded from the calculations. For all of the systems and conditions studied, three intramolecular RDF peaks are found at C-C separations of: $d_1 \approx 3.2$ Å, $d_2 \approx 3.9$ Å and $d_3 \approx 5.1$ Å (see 6). The d_1 and d_2 peaks can be mostly attributed to C atoms separated by three bonds in gauche and trans conformations respectively. The latter of these is far more intense, indicating most of the chains are in extended conformations. The d_3 peak is mostly due to C atoms separated by four bonds, and its intensity further suggests that the chains are mostly extended conformations. This observation is consistent with the trends shown previously for $\langle R^2 \rangle / (N_{\text{bonds}})^2$ (Figure 3).

There are additional peaks at larger distances in Figure 5, which are indicative of long-range order and more solid-like films. These peaks are more evident at higher pressure and lower sliding velocity, suggesting more solid-like films under these conditions. Moreover, comparing the size of the d_1 and d_2 peaks in Figure 5, it is clear that there is a smaller trans/gauche ratio at high pressure and lower speed, a further indication of more solid-like films under these conditions [48]. Longer chains also appear to be more solid-like compared to shorter chains, in agreement with previous confined NEMD simulations [9].

Figure 7 shows the atomic mass density profile in the z-dimension and x-velocity profile in the z-dimension profiles for the shortest and longest chains ($C_{16} - C_{60}$) and lowest and highest pressures ($0.5 - 1.5$ GPa) and sliding velocities ($10 - 100$ m s^{-1}) studied.

The mass density profiles in Figure 7 show the through-thickness layering of the fluids, which is strongest close to the walls. Generally, longer chains (C_{60} in blue) show stronger layering compared to shorter chains (C_{16} in purple), suggesting they form more solid-like films [16]. Comparing Figure 7a with 7b and Figure 7c with 7d shows that the films become less layered (particularly in the centre of
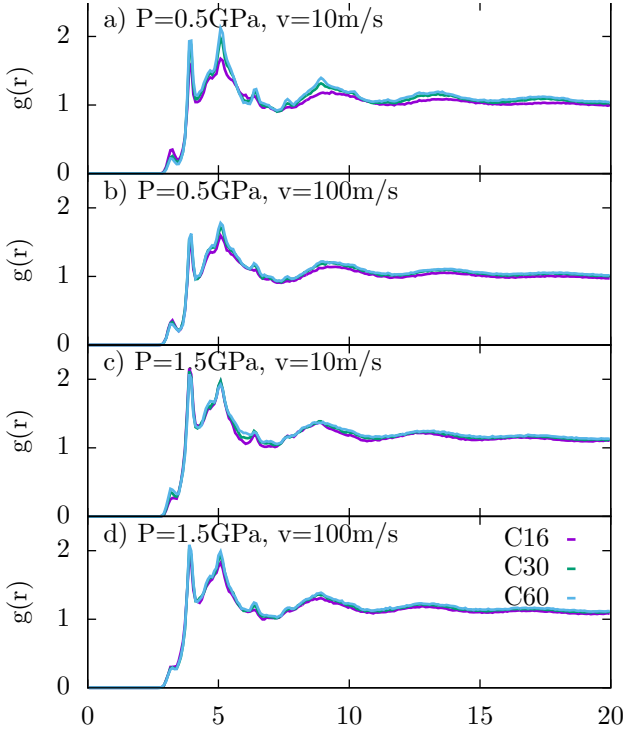
Figure 5: Radial Distribution Function $g(r)$ (RDF) measured during the steady state of the simulations for three different chain lengths: C16, C30 and C60. a) $0.5\,\mathrm{GPa}$, $10\,\mathrm{m\,s^{-1}}$, b) $0.5\,\mathrm{GPa}$, $100\,\mathrm{m\,s^{-1}}$, c) $1.5\,\mathrm{GPa}$, $10\,\mathrm{m\,s^{-1}}$ and d) $1.5\,\mathrm{GPa}$, $100\,\mathrm{m\,s^{-1}}$.
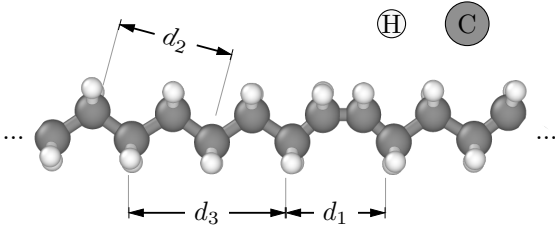
Figure 6: Distances d_1, d_2 and d_3 between pairs of carbon atoms corresponding to the first three peaks of the radial distribution functions for all the systems.

the film), and thus more liquid-like at higher sliding velocity. Comparing Figure 7a with 7c and Figure 7b with 7d shows that the films become more layered and thus more solid-like at higher pressure.

The velocity profiles show deviations from planar Couette flow at the onset of shear for several of the systems and conditions studied; however, for the majority of systems and conditions (not shown), a Couette profile develops once a nonequilibrium steady state is reached (see Appendix). Figure 7 shows steady state velocity profiles for the systems and conditions which show deviations from planar Couette flow. At low sliding velocity and low pressure (Figure 7a), the flow for C_{16} (purple) remains Couette-like, whereas C_{60} (blue) shows central localisation (CL). CL describes the outer solid-like regions of the fluid moving at the same velocity as the proximal walls with only the centre of the film being sheared [13]. The transition from Couette flow to CL has been observed for viscous polymers using in-contact photoluminescence experiments under EHL conditions [49]. It has also been observed in previous NEMD simulations of atomic fluids [13, 14, 15] as well as alkanes and traction fluids [16] under EHL conditions. At low sliding velocity and high pressure, (Figure 7c), C_{16} again shows Couette flow while C_{60} shows plug slip (PS). Here, the central part of the film becomes solid-like and shear is localized near (but not at) the fluid-wall interface [13]. The transition from Couette flow to PS has been observed for viscous polymers using in-contact photoluminescence experiments under EHL conditions [50]. The transition from CL to PS with increasing pressure has been observed in previous NEMD simulations of atomic fluids [13, 14, 15] and traction fluids [16]. At high sliding velocity, linear velocity profiles are recovered due to melting of the solid-like regions. At high sliding velocity and low pressure (Figure 7b), a small amount of boundary slip at the fluid-wall interface (slip length ¡ 1 nm) is observed for both C_{16} and C_{60}, in agreement with previous NEMD simulations of thinner films [8, 51]. The slip length increases with increasing pressure (Figure 7d) as has been observed in previous NEMD simulations [51] and in-contact photoluminescence experiments [52].

3.3. Friction

Figure 8 shows that shear stress increases linearly with increasing pressure. For all of the the systems and conditions studied, there is an approximately zero intercept in Figure 8. This suggests that it appropriate to calculate the friction coefficient, μ, using the AmontonsCoulomb law under the high load approximation; $F_L/F_N = F_0/F_N + \mu \approx \mu$, where F_L and F_N are respectively the mean lateral force (or shear stress) and normal force acting on the outer layer of atoms in each slab in response to the fluid, and F_0 is the load-independent Derjaguin offset representing adhesive surface forces [16].

Figure 9 shows the change in the shear stress, σ, with logarithmic sliding velocity and Figure 10 shows the same data as a friction coefficient, μ. In the ranges studied, σ
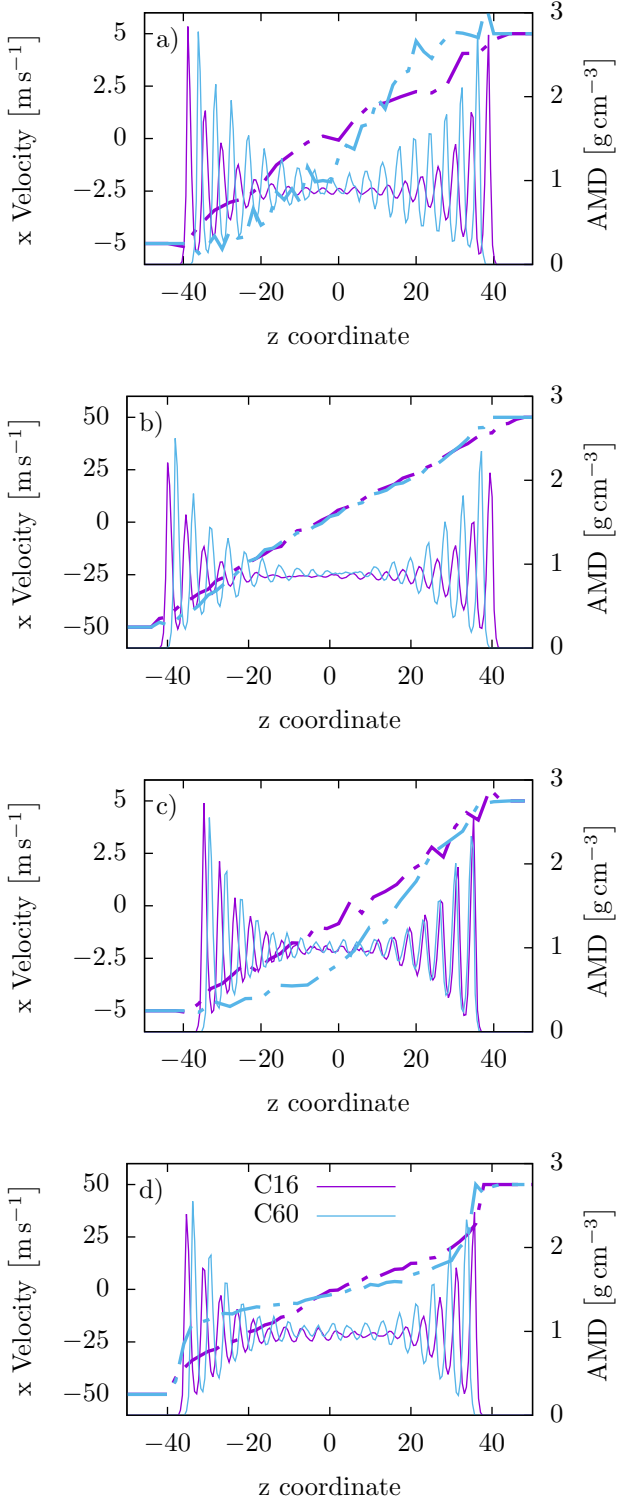
Figure 7: Velocity (solid lines) and mass density (dotted lines) measured during the steady state of the simulations for two different chain lenghts: C16 and C60. a) 0.5 GPa, 10 m s^{-1}, b) 0.5 GPa, 100 m s^{-1}, c) 1.5 GPa, 10 m s^{-1} and d) 1.5 GPa, 100 m s^{-1}
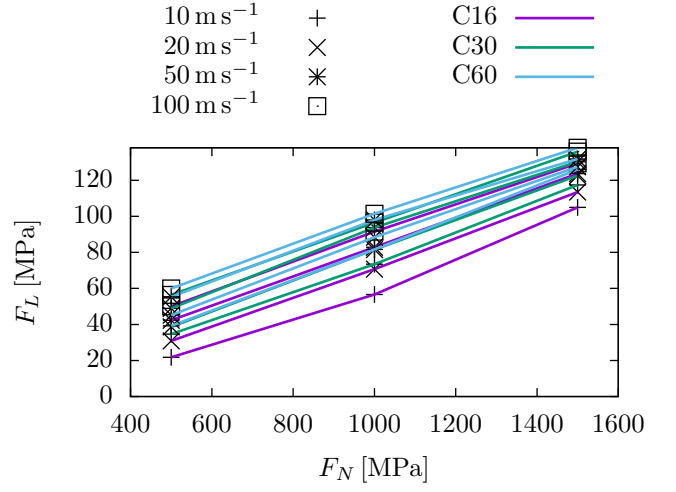

Figure 8: Lateral (friction) force, F_L, as a function of the applied pressure, F_N, on the outer layer of atoms in the top and bottom slabs measured after reaching steady stat
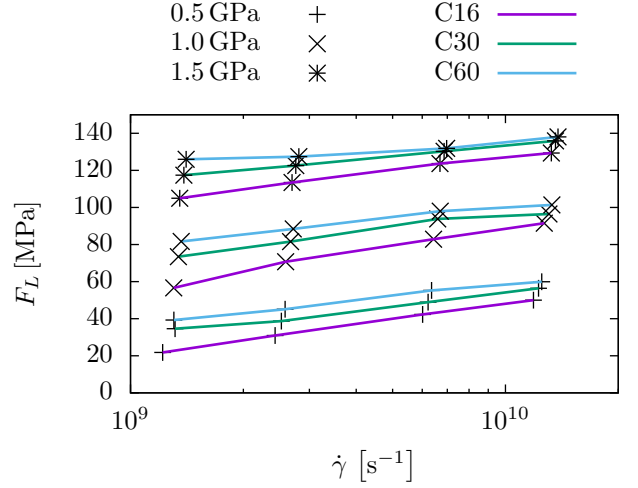

Figure 9: Shear stress as a function of the shear rate ($\dot{\gamma}$) measured after reaching steady state. Error bars, calculated from the standard deviation between the trajectory time-averages, are omitted for clarity, but are of a similar size to the symbols.
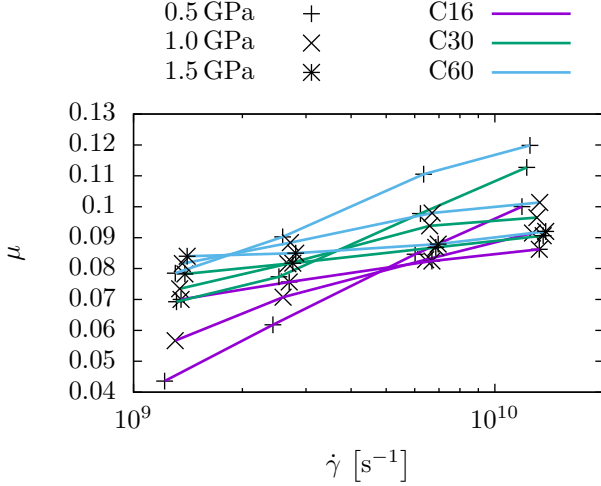
Figure 10: Friction coefficient μ as a function of the shear rate ($\dot{\gamma}$) measured after reaching steady state.

is more sensitive to the pressure than the chain length, particularly at high shear rates. In general, longer chains give higher σ than shorter chains, as expected due to their higher bulk viscosity [53]. This trend has also been observed in previous NEMD simulations of thinner films at lower pressure [6, 7, 8, 10]. The difference in σ between chain lengths decreases with increasing shear rate, such that they are almost identical at the highest shear rate studied ($\approx 10^{10}\,\mathrm{s}^{-1}$). Tribology experiments [16, 53] and engineering components [40] operate at lower shear rates than those accessible through NEMD simulations [2]. A larger increase in σ with increasing chain length can be expected under these lower shear rates than was observed here.

At low pressure, σ increases linearly with the logarithmic shear rate, as is commonly observed for lubricants in macroscopic EHL friction experiments [16]. Such behaviour has also been observed in previous NEMD simulations of linear C_{20} confined (6 molecular layers) between polymer-like surfaces at low pressure ($10\,\mathrm{MPa}$) [8]. At intermediate pressure, the σ is relatively independent of the velocity, in line with Coulomb's law for dry friction. The transition to this behaviour, above the limiting shear stress, has been observed for several model lubricants in macroscopic friction experiments [54]. Similar behaviour has also been observed in previous NEMD simulations of linear C_{60} confined (6 molecular layers) between polymer-like surfaces at low pressure ($10\,\mathrm{MPa}$) [8]. At high pressure, there is a reduction of the shear stress with increasing sliding velocity, particularly for longer chains. Such behaviour has been observed for single component atomic fluids at high pressure, where the flow profiles become non-linear due to nonequilibrium phase transitions within the fluid film [13, 14, 15].

In this study, non-linear flow profiles appear at the

onset of shear for several of the systems and conditions studied; however, a Couette profile usually develops once a nonequilibrium steady state is reached (see Appendix). Although non-linear flow persists into the steady state for some of the systems and conditions studied (Figure 7), most of the flow profiles are Couette-like, suggesting that the friction-velocity behaviour is driven by different mechanisms those observed for atomic fluids [13, 14, 15].

The decrease in σ with increasing shear rate in this study is due to a combination of factors. Firstly, boundary slip occurs at the highest shear rates studied (Figure 7), which is well known to reduce friction [8, 10]. Secondly, the increase of the temperature at high shear rates decreases the fluid viscosity and leads to more liquid-like films. The reduction in $\langle P_2^{xz} \rangle$ and $\langle R^2 \rangle$ with increasing shear rate (Figures 3 and 4) indicate that the chains are less elongated and less orientated with the flow direction, suggesting more liquid-like behaviour. The radial distribution functions (RDFs) shown in Figure 5) show that there is less long range order at higher shear rates, further suggesting a more liquid-like film. The more liquid-like films formed at high shear rates are easier to shear than the solid-like ones at low shear rates, resulting in a lower σ. Figure 11 shows the change in temperature with logarithmic shear rate. At the lowest shear rate studied, the temperature in the fluid region is the same as the thermostatted surfaces ($353\,\mathrm{K}$). As predicted by the Archard equation for EHL temperature rise [55], there is a linear increase in temperature with increasing shear rate (inset in Figure 11). The temperature rise is larger at higher pressure [55] (owing to the higher friction), but is insensitive to chain length. The temperature rises are much larger than previous NEMD simulations of branched alkanes under similar conditions [16] owing to the stronger harmonic bonds between the surface atoms, which leads to less efficient phononic dissipation.

The μ values shown in Figure 10 are of a similar magnitude, and show the same trends to those observed in previous NEMD simulations of atomic fluids [14], linear alkanes (C_{16}) [51] and branched alkanes [16] under EHL conditions. Specifically, increasing pressure decreases the slope of the increase of μ with logarithmic shear rate. As a result, at high shear rates, μ is higher at low pressure than at high pressure; an unusual observation. The structure and flow results in Figures 5, 7, and 11 suggest that the decrease can be ascribed to shear heating, more liquid-like films, and the onset of slip at high shear rates.

4. Conclusions

In this study, the behaviour of n-alkane films confined (≥ 16 molecular layers) and sheared between atomically-smooth hematite slabs has been investigated under EHL conditions using NEMD simulations. The effect of the alkane chain length ($C_{16} - C_{60}$), applied pressure ($0.5 - 1.5$ GPa), and shear rate ($10^9 - 10^{10}$ s^{-1}) on the chain ex-
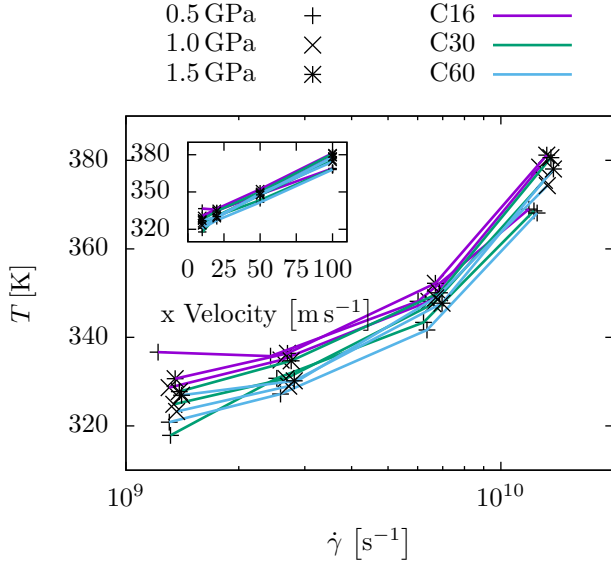
Figure 11: Temperature of the fluid region as a function of the shear rate ($\dot{\gamma}$) measured after reaching steady state. Error bars, calculated from the standard deviation between the trajectory time-averages, are omitted for clarity, but are of a similar size to the symbols.

tension and orientation, film structure and flow, and friction have been studied.

Starting from artificially ordered chains, a heat-quench cycle was used to equilibrate the systems. It was ensured that the end-to-end distance and radius of gyration reached a steady state. It was also ensured that the chains moved at least their own size by monitoring the MSD. After shear was applied, the end-to-end distance, segmental orientation, and friction were monitored to determine when a nonequilibrium steady state had been attained. The simulations agreed with previous experiments which suggested that the evolution to steady-state sliding in alkane films is governed by the sliding distance rather than the time.

At higher pressure, the films show more layering and ordering in the mass density profiles and RDF respectively, suggesting that they become more solid-like. Conversely, at higher shear rates, the chains become less elongated, aligned, layered, and ordered; indicating the films become more liquid-like as the temperature of the film increases. Longer chains are generally more solid-like, in accordance with their lower melting point.

For all of the systems and conditions studied, the shear stress increases linearly with increasing pressure. Longer chains, with higher viscosity give higher friction, particularly at low shear rates where the films are more solid-like. For short chains, the flow remains mostly Couette-like under all of the conditions studied, with some boundary slip at the highest shear rates studied. However, long chains show rich nonequilibrium phase behaviour; at low shear rates, the CL to PS transition was observed whilst at high

shear rates, boundary slip occurs.

Friction is generally more sensitive to pressure than chain length in the ranges studied. At low pressure, friction increases linearly with logarithmic shear rate, as is commonly observed for lubricants in experiments and simulations. At intermediate pressure, friction becomes insensitive to shear rate, which is indicative of reaching the limiting shear stress. At high pressure, friction decreases with increasing shear rate due to large temperature rises, shear-induced melting, and boundary slip.

Acknowledgments

Bibliography

[1] H. Spikes and Z. Jie, "History, origins and prediction of elasto-hydrodynamic friction," *Tribology Letters*, vol. 56, no. 1, pp. 1–25, 2014.

[2] J. P. Ewen, D. M. Heyes, and D. Dini, "Advances in nonequilibrium molecular dynamics simulations of lubricants and additives," *Friction*, pp. 10.1007/s40544–018–0207–9, feb 2018.

[3] S. Granick, "Motions and Relaxations of Confined Liquids," *Science*, vol. 253, pp. 1374–1379, sep 1991.

[4] P. A. Thompson, G. S. Grest, and M. O. Robbins, "Phase transitions and universal dynamics in confined films," *Physical Review Letters*, vol. 68, pp. 3448–3451, jun 1992.

[5] P. A. Thompson and M. O. Robbins, "Shear flow near solids: Epitaxial order and flow boundary conditions," *Physical Review A*, vol. 41, pp. 6830–6837, jun 1990.

[6] A. Koike and M. Yoneya, "Chain Length Effects on Frictional Behavior of Confined Ultrathin Films of Linear Alkanes under Shear," *The Journal of Physical Chemistry B*, vol. 102, pp. 3669–3675, may 1998.

[7] I. M. Sivebaek, V. N. Samoilov, and B. N. J. Persson, "Frictional properties of confined polymers," *The European Physical Journal E*, vol. 27, pp. 37–46, sep 2008.

[8] I. M. Sivebaek, V. N. Samoilov, and B. N. J. Persson, "Velocity Dependence of Friction of Confined Hydrocarbons," *Langmuir*, vol. 26, pp. 8721–8728, jun 2010.

[9] I. M. Sivebaek, V. N. Samoilov, and B. N. J. Persson, "Effective Viscosity of Confined Hydrocarbons," *Physical Review Letters*, vol. 108, p. 036102, jan 2012.

[10] D. Savio, N. Fillot, P. Vergne, and M. Zaccheddu, "A Model for Wall Slip Prediction of Confined n-Alkanes: Effect of Wall-Fluid Interaction Versus Fluid Resistance," *Tribology Letters*, vol. 46, pp. 11–22, apr 2012.

[11] M. O. Robbins and E. D. Smith, "Connecting Molecular-Scale and Macroscopic Tribology ," *Langmuir*, vol. 12, pp. 4543–4547, jan 1996.

[12] J. Van Alsten and S. Granick, "Molecular Tribometry of Ultra-thin Liquid Films," *Physical Review Letters*, vol. 61, pp. 2570–2573, nov 1988.

[13] D. M. Heyes, E. R. Smith, D. Dini, H. A. Spikes, and T. A. Zaki, "Pressure dependence of confined liquid behavior subjected to boundary-driven shear," *The Journal of Chemical Physics*, vol. 136, p. 134705, apr 2012.

[14] C. Gattinoni, D. M. Heyes, C. D. Lorenz, and D. Dini, "Traction and nonequilibrium phase behavior of confined sheared liquids at high pressure," *Physical Review E*, vol. 88, p. 052406, nov 2013.

[15] S. Maćkowiak, D. M. Heyes, D. Dini, and A. C. Brańka, "Non-equilibrium phase behavior and friction of confined molecular films under shear: A non-equilibrium molecular dynamics study," *The Journal of Chemical Physics*, vol. 145, p. 164704, oct 2016.

[16] J. P. Ewen, C. Gattinoni, J. Zhang, D. M. Heyes, H. A. Spikes, and D. Dini, "On the effect of confined fluid molecular structure on nonequilibrium phase behaviour and friction," *Physical Chemistry Chemical Physics*, vol. 19, no. 27, pp. 17883–17894, 2017.

[17] S. Plimpton, "Fast Parallel Algorithms for Short-Range Molecular Dynamics," *Journal of Computational Physics*, vol. 117, pp. 1–19, mar 1995.

[18] J. P. Ewen and S. Echeverri Restrepo, "LAMMPS_bulider doi.org/10.5281/zenodo.1043868," 2017.

[19] J. P. Ewen, S. Echeverri Restrepo, N. Morgan, and D. Dini, "Nonequilibrium molecular dynamics simulations of stearic acid adsorbed on iron surfaces with nanoscale roughness," *Tribology International*, vol. 107, pp. 264–273, mar 2017.

[20] A. I. Jewett, Z. Zhuang, and J.-E. Shea, "Moltemplate a Coarse-Grained Model Assembly Tool," *Biophysical Journal*, vol. 104, p. 169a, jan 2013.

[21] A. Hjorth Larsen, J. Jørgen Mortensen, J. Blomqvist, I. E. Castelli, R. Christensen, M. Dułak, J. Friis, M. N. Groves, B. Hammer, C. Hargus, E. D. Hermes, P. C. Jennings, P. Bjerre Jensen, J. Kermode, J. R. Kitchin, E. Leonhard Kolsbjerg, J. Kubal, K. Kaasbjerg, S. Lysgaard, J. Bergmann Maronsson, T. Maxson, T. Olsen, L. Pastewka, A. Peterson, C. Rostgaard, J. Schiøtz, O. Schütt, M. Strange, K. S. Thygesen, T. Vegge, L. Vilhelmsen, M. Walter, Z. Zeng, and K. W. Jacobsen, "The atomic simulation environmenta Python library for working with atoms," *Journal of Physics: Condensed Matter*, vol. 29, p. 273002, jul 2017.

[22] M. L. Gee, P. M. McGuiggan, J. N. Israelachvili, and A. M. Homola, "Liquid to solidlike transitions of molecularly thin films under shear," *The Journal of Chemical Physics*, vol. 93, pp. 1895–1906, aug 1990.

[23] Z. Liang, L. Chen, M. S. Alam, S. Zeraati Rezaei, C. Stark, H. Xu, and R. M. Harrison, "Comprehensive chemical characterization of lubricating oils used in modern vehicular engines utilizing GC GC-TOFMS," *Fuel*, vol. 220, pp. 792–799, may 2018.

[24] W. L. Jorgensen, D. S. Maxwell, and J. Tirado-Rives, "Development and Testing of the OPLS All-Atom Force Field on Conformational Energetics and Properties of Organic Liquids," *Journal of the American Chemical Society*, vol. 118, pp. 11225–11236, jan 1996.

[25] S. W. I. Siu, K. Pluhackova, and R. A. Böckmann, "Optimization of the OPLS-AA Force Field for Long Hydrocarbons," *Journal of Chemical Theory and Computation*, vol. 8, pp. 1459–1470, apr 2012.

[26] J. P. Ewen, C. Gattinoni, F. M. Thakkar, N. Morgan, H. A. Spikes, and D. Dini, "A comparison of classical force-fields for molecular dynamics simulations of lubricants," *Materials*, vol. 9, p. 651, aug 2016.

[27] H. Docherty and P. T. Cummings, "Direct evidence for fluidsolid transition of nanoconfined fluids," *Soft Matter*, vol. 6, no. 8, p. 1640, 2010.

[28] J.-P. Ryckaert, G. Ciccotti, and H. J. Berendsen, "Numerical integration of the cartesian equations of motion of a system

with constraints: molecular dynamics of n-alkanes," *Journal of Computational Physics*, vol. 23, pp. 327–341, mar 1977.

[29] I.-C. Yeh and M. L. Berkowitz, "Ewald summation for systems with slab geometry," *The Journal of Chemical Physics*, vol. 111, pp. 3155–3162, aug 1999.

[30] S. J. Oh, D. Cook, and H. Townsend, "Characterization of Iron Oxides Commonly Formed as Corrosion Products on Steel," *Hyperfine Interactions*, vol. 112, no. 1/4, pp. 59–66, 1998.

[31] E. N. Maslen, V. A. Streltsov, N. R. Streltsova, and N. Ishizawa, "Synchrotron X-ray study of the electron density in α-Fe 2 O 3," *Acta Crystallographica Section B Structural Science*, vol. 50, pp. 435–441, aug 1994.

[32] H. Berro, N. Fillot, and P. Vergne, "Molecular dynamics simulation of surface energy and ZDDP effects on friction in nano-scale lubricated contacts," *Tribology International*, vol. 43, pp. 1811–1822, oct 2010.

[33] T. Schneider and E. Stoll, "Molecular-dynamics study of a three-dimensional one-component model for distortive phase transitions," *Physical Review B*, vol. 17, pp. 1302–1322, feb 1978.

[34] D. Brown, J. H. R. Clarke, M. Okuda, and T. Yamazaki, "A molecular dynamics study of chain configurations in n alkanelike liquids," *The Journal of Chemical Physics*, vol. 100, pp. 1684–1692, jan 1994.

[35] R. Auhl, R. Everaers, G. S. Grest, K. Kremer, and S. J. Plimpton, "Equilibration of long chain polymer melts in computer simulations," *The Journal of Chemical Physics*, vol. 119, pp. 12718–12728, dec 2003.

[36] S. Y. Liem, D. Brown, and J. H. R. Clarke, "Investigation of the homogeneous-shear nonequilibrium-molecular-dynamics method," *Physical Review A*, vol. 45, pp. 3706–3713, mar 1992.

[37] S. Bernardi, B. D. Todd, and D. J. Searles, "Thermostating highly confined fluids," *The Journal of Chemical Physics*, vol. 132, p. 244706, jun 2010.

[38] X. Yong and L. T. Zhang, "Thermostats and thermostat strategies for molecular dynamics simulations of nanofluidics," *The Journal of Chemical Physics*, vol. 138, p. 084503, feb 2013.

[39] K. Griesbaum, A. Behr, D. Biedenkapp, H.-W. Voges, D. Garbe, C. Paetz, G. Collin, D. Mayer, and H. Höke, "Hydrocarbons," in *Ullmann's Encyclopedia of Industrial Chemistry*, Weinheim, Germany: Wiley-VCH Verlag GmbH & Co. KGaA, jun 2000.

[40] R. I. Taylor, B. R. De Kraker, A. Morina, A. Neville, and T. Liskiewicz, "Shear rates in engines and implications for lubricant design," *Proceedings of the Institution of Mechanical Engineers, Part J: Journal of Engineering Tribology*, vol. 231, no. 9, pp. 1106–1116, 2017.

[41] B. Erman and L. Monnerie, "Theory of segmental orientation in amorphous polymer networks," *Macromolecules*, vol. 18, pp. 1985–1991, oct 1985.

[42] C. Drummond and J. Israelachvili, "Dynamic behavior of confined branched hydrocarbon lubricant fluids under shear," *Macromolecules*, vol. 33, no. 13, pp. 4910–4920, 2000.

[43] S. Cho, S. Jeong, J. M. Kim, and C. Baig, "Molecular dynamics for linear polymer melts in bulk and confined systems under shear flow," *Scientific Reports*, no. July, pp. 1–9, 2017.

[44] S. Jeong, J. M. Kim, and C. Baig, "Effect of Chain Orientation and Stretch on the Stress Overshoot of Entangled Polymeric Materials under Start-Up Shear," *Macromolecules*, vol. 50, no. 8, pp. 3424–3429, 2017.

[45] S. T. Cui, S. a. Gupta, P. T. Cummings, and H. D. Cochran, "Molecular dynamics simulations of the rheology of normal decane, hexadecane, and tetracosane," *Journal Of Chemical Physics*, vol. 105, no. 3, pp. 1214–1220, 1996.

[46] P. Padilla and S. Toxvaerd, "Fluid n decane undergoing planar Couette flow," *The Journal of Chemical Physics*, vol. 97, pp. 7687–7694, nov 1992.

[47] C. Drummond, N. Alcantar, and J. Israelachvili, "Shear alignment of confined hydrocarbon liquid films," *Physical Review E - Statistical Physics, Plasmas, Fluids, and Related Interdisciplinary Topics*, vol. 66, no. 1, pp. 1–6, 2002.

[48] G. Kavitha and C. Narayana, "Raman Spectroscopic Investiga-

tions of Pressure-Induced Phase Transitions in n-Hexane," *The Journal of Physical Chemistry B*, vol. 111, pp. 14130–14135, dec 2007.

[49] B. Galmiche, A. Ponjavic, and J. S. S. Wong, "Flow measurements of a polyphenyl ether oil in an elastohydrodynamic contact," *Journal of Physics: Condensed Matter*, vol. 28, p. 134005, apr 2016.

[50] A. Ponjavic, L. di Mare, and J. S. S. Wong, "Effect of pressure on the flow behavior of polybutene," *Journal of Polymer Science Part B: Polymer Physics*, vol. 52, pp. 708–715, may 2014.

[51] T. D. Ta, A. K. Tieu, H. Zhu, B. Kosasih, Q. Zhu, and H. T. Phan, "The structural, tribological, and rheological dependency of thin hexadecane film confined between iron and iron oxide surfaces under sliding conditions," *Tribology International*, vol. 113, no. December 2016, pp. 26–35, 2017.

[52] A. Ponjavic and J. S. S. Wong, "The effect of boundary slip on elastohydrodynamic lubrication," *RSC Adv.*, vol. 4, no. 40, pp. 20821–20829, 2014.

[53] J. Zhang, A. Tan, and H. Spikes, "Effect of Base Oil Structure on Elastohydrodynamic Friction," *Tribology Letters*, vol. 65, p. 13, mar 2017.

[54] L. Martinie and P. Vergne, "Lubrication at Extreme Conditions: A Discussion About the Limiting Shear Stress Concept," *Tribology Letters*, vol. 63, p. 21, aug 2016.

[55] J. Archard, "The temperature of rubbing surfaces," *Wear*, vol. 2, pp. 438–455, oct 1959.

[56] A. Stukowski, "Visualization and analysis of atomistic simulation data with OVITOthe Open Visualization Tool," *Modelling and Simulation in Materials Science and Engineering*, vol. 18, p. 015012, jan 2010.

Appendix A. Definitions

Appendix A.1. Segmental Orientation

In MD simulations using atomically-detailed force-fields, the segmental orientation of n-alkane chains can be monitored through the orientation of the chemical bonds. The segmental orientation [41] of the fluid in terms of the second Legendre polynomial (P_2) is defined as:

$$\langle P_2 \rangle = \frac{3 \langle \cos^2 \alpha \rangle - 1}{2}, \quad (A.1)$$

where α is the angle between a chain segment and a reference axis. In practice, $\langle \cos^2 \alpha \rangle$ is calculated in the following way:

$$\langle \cos^2 \alpha \rangle = \frac{1}{N_{\text{bonds}}} \sum_{b=1}^{N_{\text{bonds}}} \left(\frac{\mathbf{r}_{ij}^b}{r_{ij}^b} \cdot \hat{\imath} \right)^2 \quad (A.2)$$

in which N_{bonds} is the total number of bonds, $\mathbf{r}_{ij}^b$ is the difference between the positions of the two beads that form the bond b, and $\hat{\imath}$ is the direction of the main axis.

In this study, the changes of the orientation in the shearing direction are monitored, through the segmental orientation with respect to x projected in the xz plane: P_2^{xz}. Note that, by definition, if all the chains are parallel to the shearing direction $\langle P_2^{xz} \rangle = 1$; if all the chains are perpendicular to the surfaces $\langle P_2^{xz} \rangle = -0.5$, and, interestingly, if all the chains are oriented at $45°$ or if they are randomly oriented $\langle P_2^{xz} \rangle = 0.25$

Appendix A.2. End-to-end distance

The mean square end-to-end distance of a single chain is defined as the square of the magnitude of the vector that points from one end of a chain to the other end. For a system containing several chains, the mean square end-to-end distance $(\langle R^2 \rangle)$ is given by the following equation [34]:

$$\langle R^2 \rangle = \left\langle (\mathbf{r}_1 - \mathbf{r}_N)^2 \right\rangle \quad (A.3)$$

where, for each chain, N is the number of atoms and $\mathbf{r}_i$ is the position vector of atom i.

Appendix A.3. Radius of gyration

The mean square radius of gyration $(\langle S^2 \rangle)$ is the average squared distance of each atom in the n-alkane chain from its centre of mass, as defined in the following equation [34]:

$$\langle S^2 \rangle = \frac{\left\langle \sum_{i=1}^{N} (\|\mathbf{r}_i - \mathbf{r}_{\text{com}}\|)^2 \right\rangle}{N} \quad (A.4)$$

where, for each chain, N is the number of atoms, $\mathbf{r}_i$ is the position vector of atom i and $\mathbf{r}_{\text{com}}$ is the centre of mass.

Appendix A.4. Mean squared displacement

The mean squared displacement (MSD) of an atom is a measure of the deviation between its current and its initial position. The MSD is usually averaged over the number of atoms (N) and its slope when plotted over time can be used to quantify the diffusion coefficient [35]. The MSD is defined as:

$$\text{MSD} = \frac{1}{N} \sum_{i=1}^{N} (\mathbf{r}_i(t) - \mathbf{r}_i(0))^2 \quad (A.5)$$

where $\mathbf{r}_i(t)$ is a vector containing the coordinates of atom i at time t.

Appendix A.5. Temperature

As common in NEMD simulations, the temperature of the lubricant is calculated via the kinetic energy of the atoms but excluding the velocity component in the direction of sliding (x) to avoid contributions that are not related to the thermal vibration of the atoms. The measurements are block-averaged every $100 \, \text{fs}$, the T values shown in Figure 11 are the time-averaged values from the final $1 \, \text{ns}$ of the sliding phase.

Appendix B. Equilibration

Figure B.12 shows the stages involved in the simulation procedure. Starting from an artificially ordered chains, the a heat-quench cycle is used to equilibrate the system, followed by compression and shear (see 2). Further details regarding the equilibration are shown below.

The evolution of $\langle R^2 \rangle$ and $\langle S^2 \rangle$ for C_{16}, C_{30} and C_{60} at $2000 \, \text{K}$ are presented on the main part of Figures B.13

and B.14. For the case of C_{60}, which has lower diffusivity, these two quantities reach a steady state after approximately 2×10^5 steps (0.2 ns). The insets of the figures show the evolution of the same quantities after reducing the temperature to 353 K; after 1×10^7 steps (10 ns), both $\langle R^2 \rangle$ and $\langle S^2 \rangle$ have reached their equilibrium values for the three chain lengths considered.

The last criterion, is based on the fact that systems of long chain alkanes that are not properly equilibrated can present deformation on short length scales, and this deformation is only relaxed after the chains have moved at least their own size [35]. In order to verify this, the mean squared displacement (MSD) for the individual atoms (MSD_{atom}) and for the centre of mass of the n-alkane chains (MSD_{CG}) were followed during equilibration.

Figure B.15 shows the MSD_{atom} and MSD_{CG} for the three different systems. The main plot is dedicated to the evolution at 2000 K, with the inset showing the evolution at 353 K. Note that due to the artificial way that the chains are first introduced into the system (see Figure B.12), the diffusivity of the longer chains is initially higher than that of the shorter chains. If we take the length of a C_{60} chain to be ≈ 74 Å (the angle between the C-C bonds is 109.5° and the C-C distance equal to 1.54 Å), it can be seen that the chains move their own size after $\approx 3 \times 10^6$ to 4×10^6 steps (3 ns to 4 ns). Taking a conservative approach, the systems are equilibrated for 1×10^7 steps (10 ns). The insets show the evolution after the temperature has been decreased; here, as expected, the slope of the MSD_{atom} and MSD_{CG} curves is shallower than at higher temperatures.

Appendix C. Transient Velocity Profiles

A representative example of transient deviations from Couette flow at the onset of shear is shown for C_{30}, 1.0 GPa and $50 \, \text{m s}^{-1}$ in Figure C.16. Most systems eventually show Couette flow, but non-linear flow persists into the steady state for some of the systems and conditions studied (Figure 7).
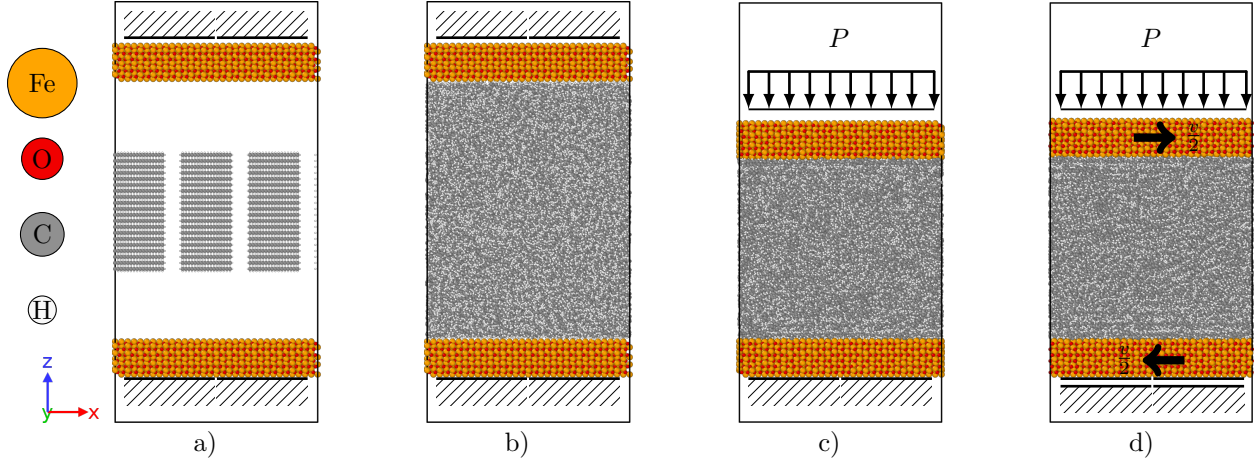
Figure B.12: General steps carried out for the preparation and NEMD simulation of each of the the systems considered in the present work. The orange atoms represent iron (Fe), the red ones oxygen (O), the gray ones carbon (C), and the white ones hydrogen (H). a) System generation. b) Equilibration. c) Compression. d) Shear.
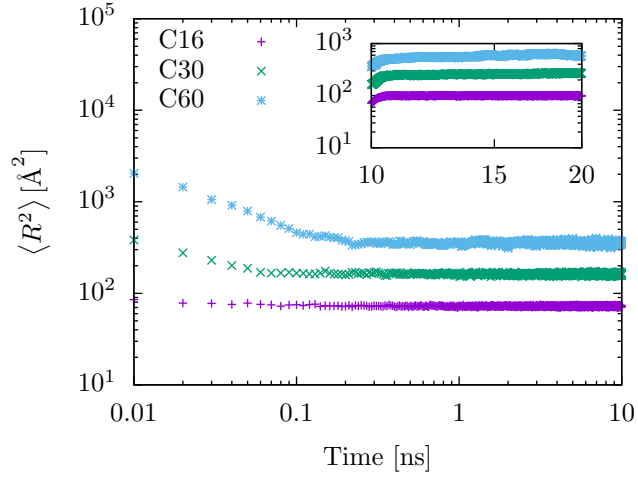

Figure B.13: Evolution of the mean square end-to-end distance $\left(\langle R^2 \rangle\right)$ during the equilibration stage for the three considered alkane lengths: C16, C30 and C60. The main plot shows the initial equilibration at 2000 K; the inset the continuation at 353 K.
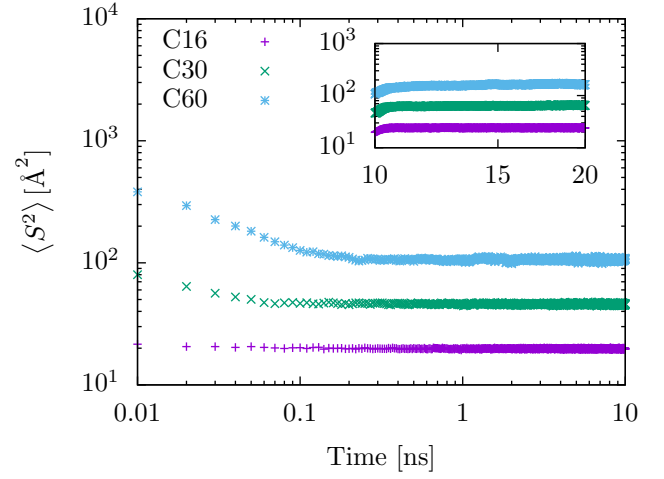

Figure B.14: Evolution of the mean square radius of gyration $\left(\langle S^2 \rangle\right)$ during the equilibration stage for the three considered alkane lengths: C16, C30 and C60. The main plot shows the initial equilibration at 2000 K; the inset the continuation at 353 K.
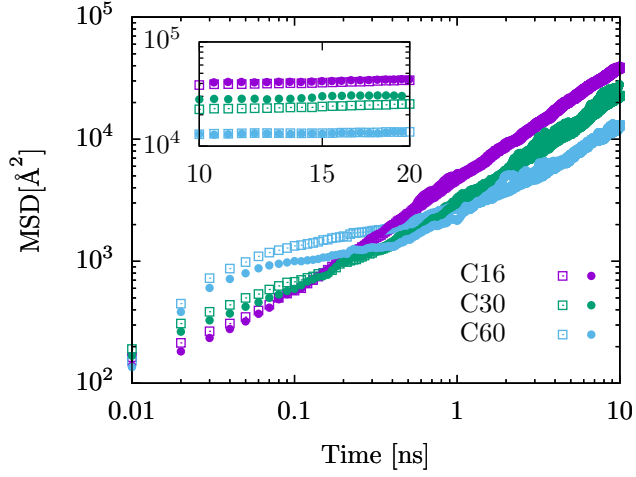
Figure B.15: Evolution of the mean squared displacement (MSD) during the equilibration stage for the three considered alkane lengths: C16, C30 and C60. The main plot shows the initial equilibration at 2000 K; the inset the continuation at 353 K. The full circles represent the mean squared displacement per atom (MSD_{atom}) while the empty squares the mean squared displacement per centre of mass of chain (MSD_{CG}).
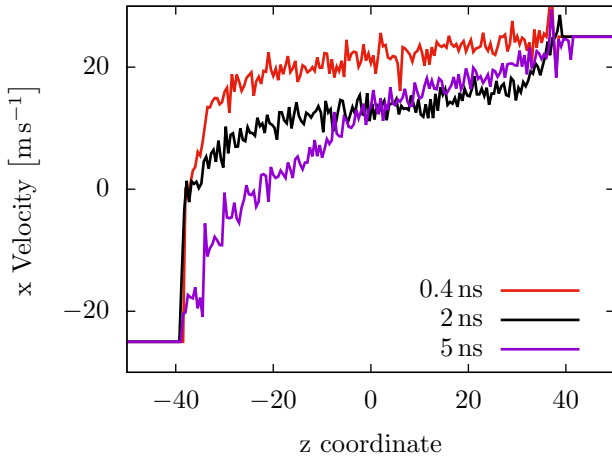

Figure C.16: Velocity profiles along x at three different times during the transient state of the simulation. Results are presented for the case of C30, $1.0\,\text{GPa}$ and $50\,\text{m}\,\text{s}^{-1}$.